

Laboratory Generated M -6 Earthquakes

GREGORY C. MCLASKEY,¹ BRIAN D. KILGORE,¹ DAVID A. LOCKNER,¹ and NICHOLAS M. BEELER¹

Abstract—We consider whether mm-scale earthquake-like seismic events generated in laboratory experiments are consistent with our understanding of the physics of larger earthquakes. This work focuses on a population of 48 very small shocks that are foreshocks and aftershocks of stick–slip events occurring on a 2.0 m by 0.4 m simulated strike-slip fault cut through a large granite sample. Unlike the larger stick–slip events that rupture the entirety of the simulated fault, the small foreshocks and aftershocks are contained events whose properties are controlled by the rigidity of the surrounding granite blocks rather than characteristics of the experimental apparatus. The large size of the experimental apparatus, high fidelity sensors, rigorous treatment of wave propagation effects, and in situ system calibration separates this study from traditional acoustic emission analyses and allows these sources to be studied with as much rigor as larger natural earthquakes. The tiny events have short (3–6 μ s) rise times and are well modeled by simple double couple focal mechanisms that are consistent with left-lateral slip occurring on a mm-scale patch of the pre-cut fault surface. The repeatability of the experiments indicates that they are the result of frictional processes on the simulated fault surface rather than grain crushing or fracture of fresh rock. Our waveform analysis shows no significant differences (other than size) between the M -7 to M -5.5 earthquakes reported here and larger natural earthquakes. Their source characteristics such as stress drop (1–10 MPa) appear to be entirely consistent with earthquake scaling laws derived for larger earthquakes.

Key words: Earthquake scaling, acoustic emission, stick–slip.

1. Introduction

Extremely small earthquakes are used to monitor mine stability (e.g. URBANCIC and TRIFU 2000) and to map hydraulic fractures and fault networks (e.g. MAXWELL *et al.* 2010). In addition, small earthquakes are believed to have similar physics to large earthquakes, and their properties are often

extrapolated to estimate the properties of larger but less frequent ones (e.g. SPOTTISWOODE and MCGARR 1975). The analysis of the smallest earthquakes requires the consideration of small wavelength radiated waves that attenuate rapidly with distance and require high speed recording equipment. Many researchers have employed sensors in deep boreholes (ABERCROMBIE 1995; JOST *et al.* 1998; PREJEAN and ELLSWORTH 2001; IMANISHI and ELLSWORTH 2006), or in mines (MCGARR 1984; GIBOWICZ *et al.* 1991; BOETTCHER *et al.* 2009; KWIA TEK *et al.* 2011) in order to determine whether the properties of these small earthquakes (M -4 to M -2) are consistent with scaling behavior observed for larger ones. KWIA TEK *et al.* (2010) studied mining induced earthquakes as small as M -4.4, while ELLSWORTH *et al.* (2007) report aftershocks of a naturally occurring M -1.8 earthquake that were as small as M -3.5. These small magnitudes imply source dimensions on the order of 100 mm.

A key parameter described in earthquake scaling studies is a stress parameter, typically termed stress drop $\Delta\sigma$, that describes how the amplitude of high frequency ground accelerations relates to the seismic moment M_0 (e.g. WALTER *et al.* 2006). If rupture properties are similar among small and large earthquakes, then we would expect to find that $\Delta\sigma$ is independent of M_0 . Site-specific studies often find that $\Delta\sigma$ appears to increase with M_0 over a limited magnitude range which might imply a breakdown in earthquake self-similarity (GIBOWICZ *et al.* 1991). However, studies that compile many datasets from a wide range of magnitudes have found no consistent scaling of $\Delta\sigma$ with moment (e.g. MCGARR 1999; IDE and BEROZA 2001) and argue that apparent scaling is due to bandwidth limitations, data selection, or inadequate treatment of path and site effects (IDE and BEROZA 2001; IDE *et al.* 2003).

¹ United States Geological Survey, 345 Middlefield Rd. MS 977, Menlo Park, CA 94025, USA. E-mail: gmclaskey@usgs.gov

In laboratory experiments, abrupt (dynamic) slip episodes on simulated faults, often referred to as ‘stick–slips’, were first suggested by BRACE and BYERLEE (1966) to be analogues of natural earthquakes. The tiny, earthquake-like tremors radiated from stick–slips and other damage processes such as microcracking are often termed acoustic emission (AE). Recordings of AE signals are used to monitor damage in laboratory experiments (e.g. LOCKNER 1993) and civil infrastructure (e.g. GROSSE and OHTSU 2008). Laboratory studies have shown many similarities between AE and earthquakes: AE signals often appear to be similar to earthquake seismograms with identifiable P and S arrivals and codas, AE magnitudes obey Gutenberg–Richter power law distributions, and they exhibit Omori-type aftershock decay sequences (LOCKNER 1993). Consequently, there is now a long history of interpreting both AE and stick–slip phenomena observed in laboratory experiments as analogues to larger earth processes (e.g. SELLERS *et al.* 2003; THOMPSON *et al.* 2009; GOEBEL *et al.* 2012; MCGARR 2012).

Unfortunately, the precise source mechanisms of AE are not typically known. AE are typically recorded with resonant piezoelectric sensors for which the precise sensor response (including coupling) is typically unknown, and this makes quantitative analysis of AE waveforms challenging (PLENKERS *et al.* 2013). As a result, even sophisticated AE analyses use simplifying assumptions regarding wave propagation, (e.g., OHTSU 1991), or employ a relative source characterization method (DAHM 1996; GROSSE *et al.* 1997; SELLERS *et al.* 2003). Studies that are able to place constraints on AE sources suggest a variety of mechanisms ranging from predominantly tensile fracture (MANTHEI 2005) to a mixture of shear, tensile, and implosive sources (ZANG *et al.* 1998; STANCHITS *et al.* 2006) or the implosive destruction of surface topography (MCLASKEY and GLASER 2011). Consequently, it is not known to what extent these tiny seismic events are consistent with our understanding of the physics of larger earthquakes. Better understanding of the physical and mechanical properties of AE and stick–slip phenomena will improve our ability to relate them to earthquake source physics and determine whether or not they are consistent with common earthquake scaling relationships.

In this paper, we quantitatively describe the source characteristics of a particular set of tiny earthquakes produced in large-scale laboratory experiments and the time-domain techniques used to analyze their radiated waves. The tiny seismic events described in this paper are associated with shear slip on a well-defined 0.4 m by 2 m planar simulated fault cut diagonally through a 1.5 m square and 0.4 m deep granite sample (Fig. 1). We believe they are the result of nondestructive frictional processes on the simulated fault surface rather than fracture of fresh rock or brittle destruction of surface topography. In addition to seismicity associated with the complete rupture of the 2 m long fault, we can identify many smaller seismic events, termed foreshocks and aftershocks (MCLASKEY and KILGORE 2013). These small shocks are the subject of the current paper, and we expect them to be similar to natural earthquakes because their source areas are contained within the interior of the simulated fault. Study of these small events allows us to extend our understanding of earthquake physics to the mm scale.

The tiny seismic events described in this paper might be termed AE because of the high frequency content of their radiation, but because the current experiments and analysis techniques differ in a number of ways from more conventional AE tests, the events reported here are termed laboratory earthquakes (LabEQs). Conventional AE detected in rock fracture experiments likely originate from grain scale (<100 μm) damage processes (i.e. LOCKNER 1993; SHAH and LABUZ 1995; ZANG *et al.* 1998; SELLERS *et al.* 2003). We roughly estimate such events to be $M < -8$, assuming a few μm of slip and a 100 μm source dimension, so it is likely that the events described here are somewhat larger ($M -7$ to $M -5.5$), and may bridge the gap between conventional AE sources and the smallest observed natural earthquakes ($M -3$ to $M -4$). As described in this paper, the large sample size, high fidelity sensors, and in situ system calibration permit a more complete consideration of wave propagation and instrument response effects, which allows the LabEQs to be studied with as much rigor as larger natural earthquakes. We present a description of the recorded waveforms and the LabEQ source locations, focal mechanisms, seismic moments, and stress drops, and the variability

Laboratory generated M -6 earthquakes

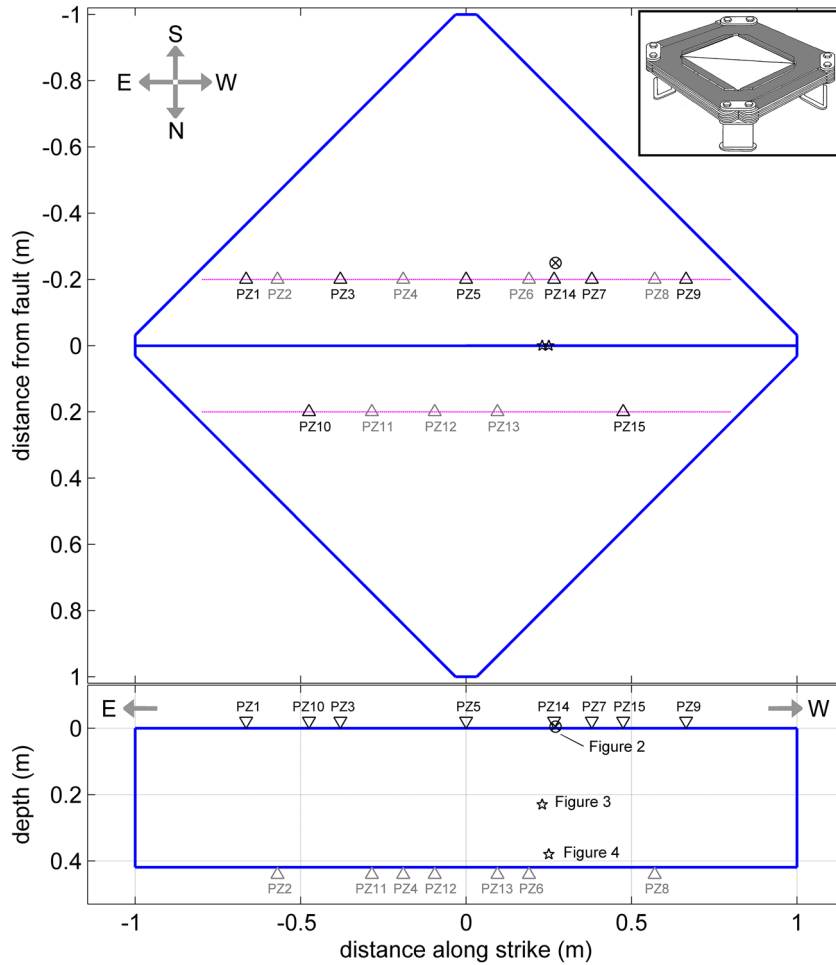


Figure 1

Schematic diagram of a top view (*upper*) and fault cross section (*lower*) of the granite sample and the locations of 15 piezoelectric sensors (PZ1–PZ15) used to record radiated ground motions. The inset in the upper right corner shows an isometric view of the sample (*white*) in the steel loading frame (*shaded*). The locations the ball impact (an ‘x’ within a circle) and LabEQs (stars) described in Figs. 2, 3, 4 are also shown

of these parameters over a population of 48 LabEQs generated on the same fault under similar experimental conditions.

Previous work indicated that these tiny events are smaller than the expected minimum length scale for unstable fault slip, and that they are triggered by nearby aseismic slip and cannot spontaneously nucleate from slow loading conditions (McLAsKEY and KILGORE 2013). The current study shows that these features are not evident from an analysis of their seismograms. The stress drops of these tiny earthquakes generally fall in the 1–10 MPa range, indicating that their properties are consistent with those of larger natural earthquakes.

2. General Description of the Experiments

Experiments were conducted on the large-scale biaxial apparatus at the USGS in Menlo Park, California (DIETERICH 1981) which accommodates a 1.5 m square and 0.4 m thick specimen composed of Sierra white granite from Raymond, California, USA, as depicted schematically in Fig. 1. A 2 m long simulated fault is cut diagonally through the sample. The fault was saw cut at the quarry and then initially roughened (in the laboratory) by lapping the two surfaces together with 30 grit silicon carbide abrasive, producing a peak-to-trough surface roughness of 80 μm , as measured with a profilometer over a

traverse of 20 mm (OKUBO and DIETERICH 1984). This sample pair (with a “rough” fault, in the terminology of OKUBO and DIETERICH 1984) has been in use for more than 25 years and has sustained hundreds of stick–slip events and probably many cm of cumulative slip without additional surface preparation, so we expect that the surface is somewhat smoother than initially reported. Operating stresses (<10 MPa) in the current experiments are well below the failure strength of the granite host rock (unconfined strength ~ 200 MPa). Consequently, there is no apparent off-fault damage and experiments can be repeated over and over again on the same samples.

Each triangular half of the sample is supported at three locations by stands (~ 30 cm in diameter) topped with Teflon pads to provide low friction coupling with the floor. A steel loading frame surrounds the four vertical sides of the specimen (upper right inset of Fig. 1), and the sample is squeezed by increasing the hydraulic fluid pressure inside four flatjacks positioned between the sample and the loading frame. The flatjacks have roughly the same area as each of the four sample sides. In a typical experiment, pressure is increased uniformly in all four flatjacks to apply the desired normal stress σ_n of 4 or 6 MPa on the fault surface. Then, under computer control, pressure is increased in one opposing pair of flatjacks and decreased in the other pair, in order to increase fault average shear stress slowly at a rate of 0.001 MPa/s while keeping fault average normal stress constant. Under this test procedure, the fault typically slips abruptly in stick–slip fashion when the average shear stress attains a value of 0.76–0.80 of the average normal stress. We refer to these global stick–slip instabilities, in which the entire fault surface undergoes dynamic failure, as dynamic slip events (DSEs). An accelerometer on the sample is used as a trigger signal such that each DSE activates the closure of a ball valve so that the volume of hydraulic fluid in the flatjacks is held constant for some time period t_{hold} after which slow shear loading resumes and the load cycle is repeated.

Fifteen Panametrics V103 piezoelectric sensors (PZ1–PZ15) are mounted 200 mm from the simulated fault on either side and on both the top and bottom surfaces of the sample (see Fig. 1). These sensors detect surface normal motions in the frequency range

of ~ 100 Hz to ~ 1 MHz and act as vertical-component seismic stations. Signals from the sensors are recorded with a high speed recording system (14 bit 5 MHz) in triggered mode for 420 ms intervals that include each DSE. In addition, capacitive slip sensors straddle the fault and measure local fault slip at 16 locations along the top surface of the sample both continuously at 100 Hz and in triggered mode for 512 ms at 1 MHz surrounding each DSE. More experimental details about the apparatus and instrumentation can be found elsewhere (OKUBO and DIETERICH 1984; BEELER *et al.* 2012; MCLASKEY and KILGORE 2013).

When a DSE occurs, the entire fault of length 2 m slips 50–150 microns. Typically, the majority of the fault slip occurs in about 3–5 ms, but some premonitory fault slip and slow afterslip usually occurs in the surrounding hundreds of ms. The premonitory slip and afterslip are predominantly aseismic, but do produce small, localized LabEQs, termed foreshocks and aftershocks, which are the subject of the current study. Unlike DSEs, these tiny LabEQs have abrupt onsets that radiate clearly defined P and S waves that can be used to calculate event locations and mechanisms. For cataloging purposes each DSE is numbered sequentially and labeled by experiment date (i.e. SE4_{Nov2012}) while foreshocks (FS) and aftershocks (AS) are labeled by their timing relative to the initiation of the DSE such as SE12_{Nov2012}FS-17 (a foreshock occurring 17 ms before the beginning of dynamic rupture of SE12) and SE12_{Nov2012}AS + 49 (an aftershock occurring 49 ms after initiation of SE12).

3. Contained Foreshocks and Aftershocks Versus DSEs

While contained stick–slip events have been produced when the stress state on the simulated fault is specifically controlled by fluid injection (Lockner *et al.* 1982), the vast majority of experiments on the current apparatus produce DSEs that rupture the entire simulated fault. For these uncontained DSEs, the free ends of the fault and the stiffness of the loading frame contribute to the energetics of the event. The stiffness of the laboratory apparatus is less

than that of a crack of equivalent area within granite, so some adjustments are required for the comparison of DSEs to natural earthquakes (e.g. MCGARR 1994, 2012; MCGARR and FLETCHER 2003). However, the small foreshocks and aftershocks described here were chosen for analysis specifically because they are contained events where nucleation, rupture, and arrest are controlled by the rigidity of the surrounding granite blocks and are not affected by characteristics of the loading frame. Indeed, with observed source durations of $<6 \mu\text{s}$, as discussed below, these events have ended before dynamic stress perturbations have traveled 25 mm from the source. We expect these contained events to be directly comparable to natural earthquakes.

We describe the characteristics of foreshocks and aftershocks produced during a set of experiments similar to those previously reported (MCLASKEY and KILGORE 2013) except that the hold time t_{hold} between DSEs was varied from 2 to 80 min, and sample average fault normal stress was held constant at either 4 MPa (SE1-12) or 6 MPa (SE13-27). From this study as well as previous studies, we note that important characteristics of the nucleation of the DSEs are sensitive to both hold time and normal stress. Some DSEs have a significant amount ($>20 \mu\text{m}$) of premonitory slip as well as afterslip. Other DSEs are more similar to those reported in MCLASKEY and KILGORE (2013) and have $<10 \mu\text{m}$ of premonitory slip and no measurable afterslip or detectable aftershocks.

The tiny LabEQs discussed here (linear dimension $<10 \text{ mm}$) are termed foreshocks and aftershocks because they always occur in close temporal proximity (typically within 500 ms) to larger DSEs that rupture the entire fault. The current dataset is consistent with previous work (MCLASKEY and KILGORE 2013) that showed that these events are driven by rapid stress changes due to nearby larger scale aseismic slip, and do not occur on their own as spontaneous slip events embedded in an otherwise-locked fault. We have searched for small events throughout the entire load cycle, but we only detect them when and where measured premonitory slip or afterslip rates exceed approximately $50 \mu\text{m/s}$. MCLASKEY and KILGORE (2013) proposed that the source area of these tiny events is smaller than a

minimum length scale for unstable slip under the conditions of homogenous fault strength and tectonic loading rates, and that the increased stressing rate caused by aseismic slip of surrounding areas is responsible for their existence. Here, we more rigorously address whether any of the unique circumstances under which these LabEQs occur might be discernible in an analysis of their radiated seismic waves.

4. Methods

For the accurate characterization of a seismic source, we must be able to isolate source effects from instrument effects and wave propagation effects, typically described by a Green's function. In conventional AE tests, thousands of individual AE are recorded, so the goal is to estimate the source locations (and possibly source mechanisms) in an automated procedure of data extraction and inversion. Even in AE tests that record full waveforms and include detailed post-processing of the data, a few incorrect wave arrival estimates, or inexact Green's functions, can produce inaccurate source location estimates (even physically unrealistic location estimates such as outside the sample), and this will cause severe biases in the focal mechanism results (LINZER 2005; MANTHEI 2005). Additionally, small sample sizes and high pressure environments limit the types of sensors that can be used and make it difficult to apply quantitative artificial sources of seismic waves for in situ verification of the transducer, transducer coupling, and recording system characteristics (MANTHEI 2005). As a consequence, most analyses rely on relative amplitudes rather than absolute measurements.

In the current experiments we record only a few (2–10) foreshocks or aftershocks before and after each SE. Instead of using automated algorithms, we carefully analyze the waveforms recorded from each LabEQ and compare them to full waveform synthetic seismograms generated from full elastodynamic Green's functions and instrument response functions obtained from calibration experiments. Signals recorded in the current experiments are amenable to rigorous analysis for four reasons: (1) There is

essentially no off-fault damage so source-to-sensor ray paths traverse intact, homogeneous, fine-grained granite with directly measurable elastic properties. (2) The large source-to-sensor path length allows different wave arrivals to separate in time by 20–50 μs , which is greater than the source duration of the small LabEQs. Consequently, P and S waves (and a few other later arriving phases such as reflections) can be clearly isolated in time and analyzed separately. The S wave phase is particularly useful for constraining focal mechanisms, and reflections are sometimes helpful for constraining source locations. (3) Both sources and sensors are located far (0.5–1 m) from the side edges of the sample so that recorded waveforms are not complicated by side reflections or interactions with the loading frame for a relatively long period of time (hundreds of μs). (4) Because the sensors used in this study are sensitive to displacement rather than velocity or acceleration, coherent pulse-shaped farfield P and S wave arrivals are readily distinguishable from higher frequency and incoherent scattered waves. These features make waveform analysis more straightforward and allow for a more robust estimation of source characteristics described below. The main challenge of this study is that seismicity is clustered in time, so small aftershocks often occur within the coda of previous events, leading to an unavoidable reduction of signal-to-noise ratio.

4.1. Wave Propagation

For frequencies below a few MHz, wavelengths are significantly larger than the grain size, and the granite samples can be well approximated as linear elastic, isotropic, and homogeneous. Consequently, wave propagation effects can be estimated theoretically by solving elastodynamic equations. We use a generalized ray theory code to calculate Green's functions (Hsu 1985). The code assumes an infinite slab geometry; therefore, Green's functions presented here include reflections off the top and bottom free surfaces of the sample (as well as direct waves, surface waves, and nearfield terms) but do not include reflections from the four vertical sides of the sample, and the fault is assumed to be transparent. The direct arrivals (P, S, Rayleigh, and nearfield components)

were checked against 3D finite element models, so we are confident in the accuracy of the synthetic seismograms for the early part of the signal. A comparison between the generalized ray theory solutions and finite element solutions is described in the appendix. We restrict our analysis to only the first few hundred microseconds of recorded signals before side reflections reach the sensors. This time of usable signal is an order of magnitude longer than typical AE recorded from cm-sized samples where reflections off the sides of the sample arrive 5–20 μs behind direct P wave arrivals and produce a 'coda' that is difficult to analyze deterministically.

4.2. Sensor Calibration and System Verification

Since theoretical Green's functions are readily obtainable for the laboratory samples, the sensors can be absolutely calibrated from theory by employing a known calibration source. The piezoelectric sensor model used in these experiments (Panametrics V103) was first calibrated when coupled to a 50 mm thick steel plate, following the methods of McLASKEY and GLASER (2012). The calibration indicated that, in the ~ 30 kHz–1 MHz frequency band, sensor output (voltage) is very nearly proportional to ground displacement. At high frequencies, the finite aperture of the sensor causes a decrease in sensitivity to incoming waves with low incidence angle (McLAsKEY and GLASER 2012). For this sensor (16 mm diameter aperture), the aperture effect becomes significant for frequencies above about 200 kHz and increases with increasing frequency such that it can cause up to a 20 dB reduction in sensitivity at 700 kHz. Based on the results of the calibration experiments, we constructed a time domain model of the impulse response function of the sensor which is used to model the modest sensor distortions included in the synthetic seismograms described below. Since this model does not include aperture effects, for this study, our reliable frequency band is limited to ~ 30 –300 kHz. The consideration of lower frequencies requires longer time windows, and the Green's functions described above are not valid for windows longer than a few hundred μs . An analysis of the LabEQ characteristics in the frequency domain, which includes the consideration of lower frequencies

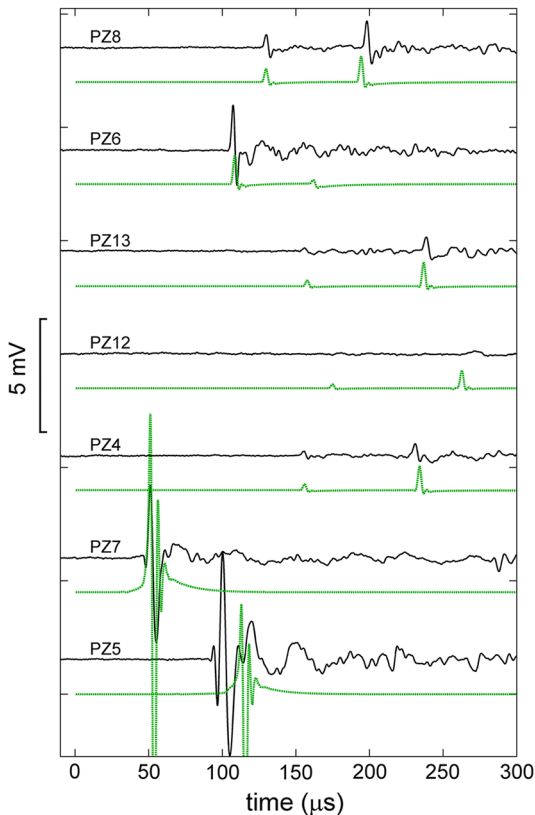


Figure 2

Unfiltered, unamplified recorded signals from the impact of a 1.00 mm glass ball dropped from a height of 1 m onto the top surface of the sample (location shown in Fig. 1). Signals from seven sensors are shown alongside synthetic seismograms (*green dotted lines*) that take into account wave propagation effects, minor sensor distortions, and a source that is represented as a 5 N force pulse with 4.5 μ s duration. Sensor output is roughly proportional to vertical surface displacement with sensitivity 20 mV/nm. Positive displacement is in the direction outward from the sample

and employs an empirical Green's function, is the subject of further study (McLAsKEY *et al.* in preparation).

In addition to the initial transducer calibration on a steel plate, we used the seismic waves radiated from a ball dropped onto the granite samples as a way to verify the properties of the sensors and recording system when under actual test conditions. Figure 2 shows recorded waveforms and synthetic seismograms from a 1.00 mm diameter glass ball dropped 1 m onto the surface of the granite sample under 5 MPa fault normal stress, which was applied to simulate the stress conditions during testing. The comparison of recorded signals and synthetic seismograms from ball

drop calibration sources at known locations is used to verify sensor coupling and sensitivity which was found to be roughly 20 mV/nm, and to calibrate our velocity model used in the Green's function code ($v_p = 4,080$ m/s and $v_s = 2,700$ m/s). The synthetic seismograms were calculated by convolving the appropriate Green's function with the sensor's impulse response function and a source function that is a single-sided pulse. This pulse is the force time history that the ball imposes on the sample. Since the ball typically bounces back to $>50\%$ of its initial drop height, the force pulse can be estimated with Hertzian theory (McLAsKEY and GLASER 2010). To estimate attenuation, we constructed a few sets of synthetic seismograms with various degrees of attenuation explicitly assumed. In this way, we roughly estimate a frequency independent quality factor $Q \sim 150$, which is generally consistent with previous estimates for Sierra white granite in our ~ 30 – 300 kHz frequency band (ULRICH *et al.* 2002). We did not include the effects of attenuation in any further analyses. Future work will include corrections for attenuation and the aperture effect.

The ball impact imposes a downward force on the top surface of the specimen, so the P wave first motion is compressional (at all azimuths) rather than dilatational. Sensors located on the bottom surface of the sample should, therefore, all have down first motions. In Figs. 2, 3, 4 and Fig. 9 positive vertical displacement is in the direction outward from the sample. For the sensors on the top surface of the sample, positive displacement is up, but for sensors located on the bottom of the sample (which are oriented upside down), positive displacement is down. The two lower traces in Fig. 2 are from sensors located on the top surface of the sample. These sensors see large amplitude Rayleigh waves and very small amplitude direct P waves. We find that these waves that travel along the free surface are poorly modeled with the synthetic seismograms, so they are excluded from our analysis.

4.3. Source Location, Focal Mechanisms, and Source Parameters

The source properties of the individual LabEQs were estimated from forward modeling by comparing

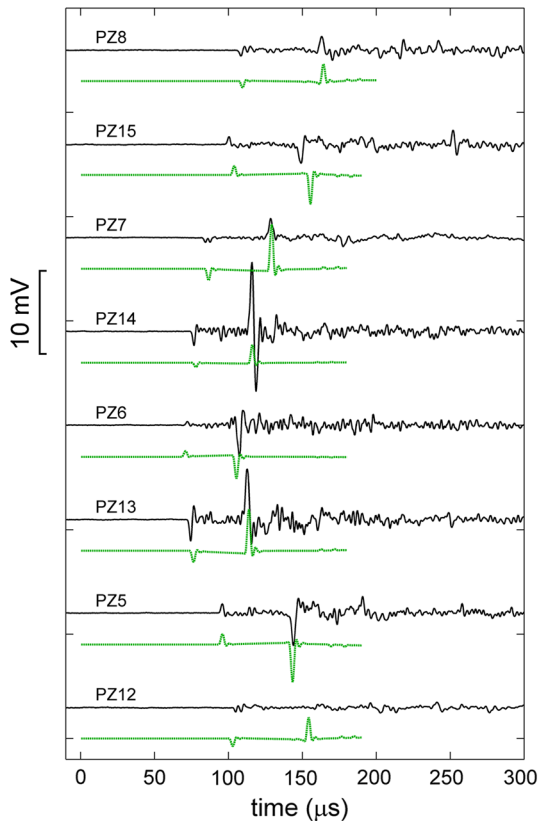


Figure 3

Unfiltered, unamplified recorded signals from **M** -6.5 LabEQ (SE25_{Nov2012} FS-13). The source location relative to sensor locations is shown in Fig. 1. Signals from eight sensors are shown alongside synthetic seismograms (*green dotted lines*) which take into account wave propagation effects, minor sensor distortions, and a source which has a left-lateral strike slip double couple focal mechanism. The current geometry and source mechanism produces P and S waves which always have opposite polarity. Sensor output is roughly proportional to vertical surface displacement with sensitivity 20 mV/nm. Positive displacement is in the direction outward from the sample

full-waveform synthetic seismograms to recorded signals. Figures 3 and 4 show raw recorded signals alongside synthetic seismograms for two well-constrained LabEQs. In our source characterization procedure, the source location is first estimated from the relative timing of arrivals for P, S, and, in some cases, reflected waves calculated from our calibrated velocity model. We estimate a ± 10 mm source location accuracy in both along-strike and depth dimensions. Accuracy is likely limited by our velocity model that assumes the granite blocks are isotropic and homogeneous. Source locations are

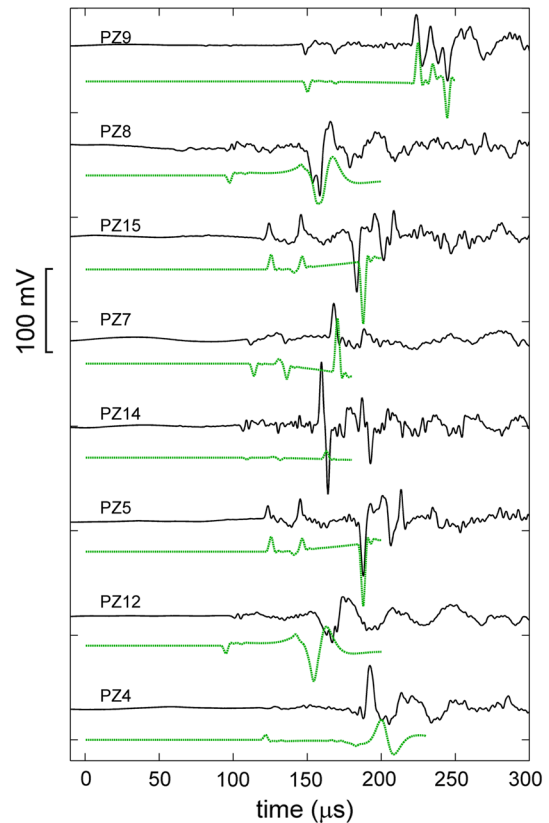


Figure 4

Same as Fig. 3, but a **M** -5.5 LabEQ (SE16_{Nov2012} FS-18). Since this LabEQ is located close to the bottom surface of the sample, initially down-going rays that reflect off the bottom free surface of the sample arrive in between the direct P and S waves on the recordings from sensors located on the top surface of the sample (PZ9, PZ15, PZ7, and PZ5)

assumed to lie on the fault plane, and the good fit to the synthetics justifies this assumption at least to ± 10 mm accuracy. The synthetic seismograms are calculated in a similar fashion to those shown in Fig. 2 (radiation pattern and minor sensor distortions are accounted for but not attenuation, Q, or sensor aperture effects) except the source is represented as a full moment tensor $M_{ij}(t)$, and we use the first spatial derivative of the Green's function. We assume that the time history of each component of $M_{ij}(t)$ is identical such that $M_{ij}(t) = m(t)M_{ij}$, where $m(t)$ is scalar seismic moment as a function of time. We estimate the focal mechanism M_{ij} from the polarities and relative amplitudes of direct P and S wave arrivals recorded by many nearby stations (typically 4–8). Finally, we estimate the width t_0 and height

\dot{m}_{\max} of a pulse-shaped moment rate function $\dot{m}(t)$ (the overdot represents a time derivative). There is some variability in source properties with angle of observation (observable in the waveforms shown in Fig. 3 and 4), but instead of estimating t_0 and \dot{m}_{\max} separately from recordings from individual sensors, these parameters (as well as M_{ij}) are estimated, in an average sense, for each event using constraints from direct P and S wave arrivals of many sensors. For these estimates, we place the most confidence in recordings from sensors whose source-to-sensor ray paths are far from nodes in the radiation pattern and predominantly travel through the interior of the sample rather than close to the free surfaces. For example, in Figs. 3 and 4, the signal recorded by sensor PZ14 is not well matched by the synthetic seismogram, but this station is close to a node in the P wave radiation pattern for these events.

5. Results and Discussion

5.1. Locations and Catalog Considerations

We analyze a catalog of 48 LabEQs, shown in Fig. 5, that could be accurately located and were separated enough in time from previous events that characteristics of pulse-shaped direct P and S wave arrivals could be estimated from the recorded signals. The LabEQs are categorized as either foreshocks (occurring before complete rupture of the 2 m long simulated fault) or aftershocks (occurring after complete rupture), denoted by circles and diamonds,

respectively, in Fig. 5. We did not analyze the many additional foreshocks and aftershocks that were detected but had extremely small amplitudes or were buried in the coda of previous events. While LabEQs did occur close to the ends of the fault, our selection criterion removes from the catalog any LabEQs located outside of the sensor array, as shown in Fig. 5. A few larger ($M > -5.0$) foreshocks with more complicated source functions (their moment rate function $\dot{m}(t)$ could not be adequately represented with a single pulse), were also excluded. These larger events are studied with frequency domain techniques reported elsewhere (McLAsKEY *et al.* manuscript in preparation).

In general, both foreshocks and aftershocks are broadly distributed across the simulated fault, and there are no obvious differences between foreshocks and aftershocks, in either focal mechanisms, magnitudes, or stress drops, as described below. When the nucleation processes of successive DSEs are very similar, the foreshock locations cluster on specific fault patches. In most cases, clustered foreshocks also have similar source characteristics, such as SE25_{Nov2012}FS-148 and SE26_{Nov2012}FS-84, two foreshocks located at 0.36 m along strike and 0.38 m depth that are both relatively high stress drop events (see Table 1). The increased variability in nucleation patterns observed in the current experiments, due to more variable value of t_{hold} , is the likely reason why less clustering of seismicity is observed in the current sets of DSEs than in a previously recorded dataset (McLAsKEY and KILGORE 2013).

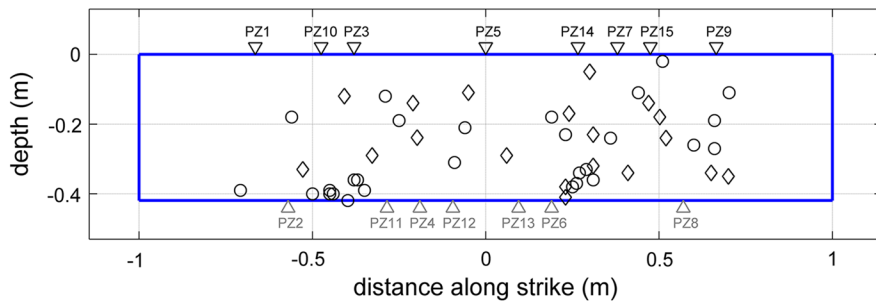


Figure 5

Fault cross section showing locations of 48 LabEQs listed in Table 1 that are foreshocks (*circles*) or aftershocks (*diamonds*) of complete rupture events on a the 2 m-long simulated fault. Locations have ± 10 mm accuracy both along strike and with depth. Events are also detected near the fault ends, but those events are excluded from the current catalogue because their location uncertainties are larger

Table 1
Forty-eight LabEQs

LabEQ name	σ_n (MPa)	Dist. along strike (m)	Depth (m)	t_0 (μ s)	\dot{m}_{\max} (kNm/s)	M_0 (Nm)	M	f_0 (kHz)	r_0 (mm)	$\Delta\sigma$ (Mpa)
SE6Nov2012 AS+12	4	-0.05	0.11	3.5	75	0.146	-6.6	286	3.5	1.47
SE7Nov2012 AS+29	4	0.52	0.24	3.5	55	0.107	-6.7	286	3.5	1.07
SE8Nov2012 AS+30	4	-0.21	0.14	4.0	55	0.122	-6.7	250	4.0	0.82
SE8Nov2012 FS-41	4	-0.06	0.21	3.5	15	0.029	-7.1	286	3.5	0.29
SE8Nov2012 FS-35	4	0.31	0.36	5.5	15	0.046	-7.0	182	5.5	0.12
SE10Nov2012 AS+19	4	0.65	0.34	5.0	350	0.974	-6.1	200	5.0	3.35
SE10Nov2012 AS+24	4	0.06	0.29	4.0	72	0.16	-6.6	250	4.0	1.08
SE10Nov2012 AS+25	4	0.41	0.34	3.0	150	0.25	-6.5	333	3.0	3.99
SE10Nov2012 AS+30	4	0.23	0.38	4.5	125	0.313	-6.4	222	4.5	1.48
SE10Nov2012 AS+47	4	0.30	0.05	2.5	30	0.042	-7.0	400	2.5	1.15
SE12Nov2012 FS-46	4	-0.50	0.40	3.5	430	0.837	-6.1	286	3.5	8.4
SE12Nov2012 FS-44	4	-0.56	0.18	3.5	40	0.078	-6.8	286	3.5	0.78
SE12Nov2012 FS-17	4	-0.29	0.12	4.0	200	0.445	-6.3	250	4.0	2.99
SE12Nov2012 FS-2	4	-0.35	0.39	4.0	60	0.134	-6.6	250	4.0	0.9
SE12Nov2012 AS+49	4	0.24	0.17	5.0	200	0.556	-6.2	200	5.0	1.92
SE12Nov2012 AS+17	4	0.47	0.14	3.0	20	0.033	-7.1	333	3.0	0.53
SE13Nov2012 FS-197	6	-0.45	0.39	4.0	100	0.223	-6.5	250	4.0	1.5
SE13Nov2012 AS+12	6	0.31	0.32	4.0	300	0.668	-6.2	250	4.0	4.49
SE13Nov2012 AS+1100	6	0.70	0.35	4.0	150	0.334	-6.4	250	4.0	2.24
SE14Nov2012 FS-13	6	-0.45	0.40	2.5	270	0.376	-6.4	400	2.5	10.3
SE14Nov2012 FS-11	6	0.29	0.33	5.0	300	0.835	-6.1	200	5.0	2.87
SE15Nov2012 FS-17	6	0.19	0.18	3.0	250	0.417	-6.3	333	3.0	6.65
SE15Nov2012 FS-14	6	-0.44	0.40	5.0	300	0.835	-6.1	200	5.0	2.87
SE16Nov2012 FS-32	6	-0.45	0.39	4.0	1,000	2.226	-5.8	250	4.0	15
SE16Nov2012 FS-23	6	-0.25	0.19	3.0	20	0.033	-7.1	333	3.0	0.53
SE16Nov2012 FS-18	6	0.25	0.38	5.5	2,160	6.61	-5.5	182	5.5	17.1
SE17Nov2012 FS-30	6	0.36	0.24	3.5	15	0.029	-7.1	286	3.5	0.29
SE17Nov2012 FS-22	6	-0.40	0.42	5.0	25	0.07	-6.8	200	5.0	0.24
SE18Nov2012 FS-183	6	-0.71	0.39	4.0	65	0.145	-6.6	250	4.0	0.97
SE18Nov2012 FS-28	6	0.70	0.11	3.5	400	0.779	-6.1	286	3.5	7.82
SE18Nov2012 FS-3	6	0.26	0.37	4.5	65	0.163	-6.6	222	4.5	0.77
SE18Nov2012 AS+11	6	-0.53	0.33	4.5	600	1.502	-5.9	222	4.5	7.09
SE18Nov2012 AS+15	6	-0.33	0.29	3.5	250	0.487	-6.3	286	3.5	4.89
SE18Nov2012 AS+17	6	-0.41	0.12	3.0	160	0.267	-6.4	333	3.0	4.26
SE18Nov2012 AS+19	6	0.50	0.18	5.0	400	1.113	-6.0	200	5.0	3.83
SE19Nov2012 AS+33	6	-0.20	0.24	3.5	14	0.027	-7.1	286	3.5	0.27
SE25Nov2012 FS-53	6	0.60	0.26	4.0	180	0.401	-6.3	250	4.0	2.69
SE25Nov2012 FS-36	6	0.51	0.02	4.0	420	0.935	-6.1	250	4.0	6.28
SE25Nov2012 FS-13	6	0.23	0.23	4.0	85	0.189	-6.5	250	4.0	1.27
SE25Nov2012 FS-148	6	-0.38	0.36	4.5	3,600	9.014	-5.4	222	4.5	42.6
SE25Nov2012 FS-104	6	-0.09	0.31	3.0	20	0.033	-7.1	333	3.0	0.53
SE26Nov2012 FS-84	6	-0.37	0.36	5.5	3,700	11.323	-5.4	182	5.5	29.3
SE26Nov2012 FS-39	6	0.27	0.34	3.0	84	0.14	-6.6	333	3.0	2.23
SE26Nov2012 FS-27	6	0.44	0.11	2.5	30	0.042	-7.0	400	2.5	1.15
SE26Nov2012 FS-8	6	0.66	0.27	5.0	40	0.111	-6.7	200	5.0	0.38
SE26Nov2012 FS-5	6	0.66	0.19	5.5	250	0.765	-6.1	182	5.5	1.98
SE26Nov2012 AS+48	6	0.31	0.23	4.5	25	0.063	-6.9	222	4.5	0.3
SE26Nov2012 AS+97	6	0.23	0.41	3.5	25	0.049	-6.9	286	3.5	0.49

5.2. Focal Mechanisms

The synthetic seismograms shown in Figs. 3 and 4 are each computed from a source that has a left-

lateral double couple focal mechanism with one of the two nodal planes oriented parallel to the fault. Sensors located on the south side of the fault and east

of the LabEQ hypocenter (PZ1-PZ6, see Fig. 1) see compressive P wave first motions, while sensors west of the hypocenter (PZ7-PZ9) see dilatational P wave first motions. Sensors located on the north side of the fault see opposite polarities. In the current geometry, the sign of the S wave first motions is always opposite that of the P wave for a double couple mechanism (Figs. 3, 4) while the ball drop source produces S waves that are the same polarity as P waves (Fig. 2). The good match between synthetic seismograms and recorded signals indicates that the LabEQs are well explained by the simple double couple mechanism. We cannot rule out the possibility of some percentage of non-double-couple components, but it cannot exceed about 20 %, otherwise the polarities and relative amplitudes of the P and S waves would be altered enough to be easily identified in the waveforms.

The vast majority of the LabEQs were well modeled by identical double couple focal mechanisms indicative of a shear dislocation on the fault. Only two of the 48 LabEQs studied had signals with P and S wave arrivals that were somewhat inconsistent with this model, but a more suitable source could not be identified.

5.3. Moment, Corner Frequencies, and Stress Drop

Estimates of source parameters t_0 and \dot{m}_{\max} derived from waveform modeling, as described in Sect. 4.3, are shown in Fig. 6 and listed in Table 1. (Note that we only estimated t_0 to the nearest 0.5 μs .) We calculate $M_0 = t_0 \dot{m}_{\max} / 2$, and for simplicity, we assume the BRUNE (1970) relationship between corner frequency and source dimension $r_0 = 2.34 * \beta / (2\pi f_0)$ and calculate stress drop $\Delta\sigma = 7/16 M_0 r_0^{-3}$. Here, corner frequency f_0 is approximated as $1/t_0$, and β is the shear wave velocity in the granite (2,700 m/s). Estimates of M_0 and $\Delta\sigma$, calculated from t_0 and \dot{m}_{\max} , are shown in Fig. 7, and reported in Table 1.

For the 48 LabEQs catalogued here, t_0 estimates range from 2.5 to 5.5 μs , which correspond to f_0 of 400–180 kHz and Brune source radii of 3–6 mm. \dot{m}_{\max} ranges from 10 to over 1,000 kNm/s and shows little correlation with t_0 . Most of the variation in M_0 , from 0.05 to 10 Nm, is due to variations in the

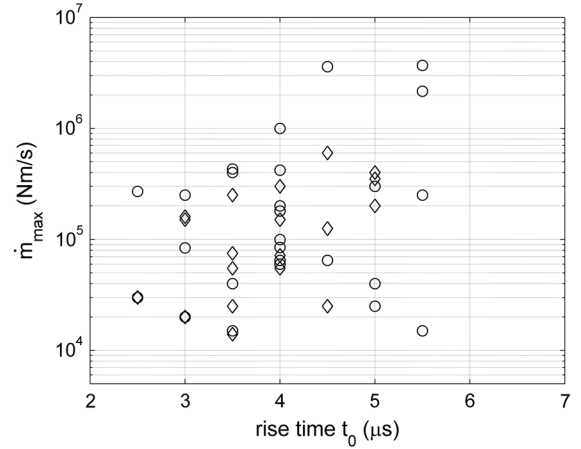


Figure 6

Width t_0 and amplitude \dot{m}_{\max} of the moment rate functions of 48 LabEQs listed in Table 1 that are foreshocks (circles) or aftershocks (diamonds) of complete rupture events on a the 2 m-long simulated fault. These parameters are estimated in the time domain from the width and amplitude of pulse-shaped direct P and S wave arrivals

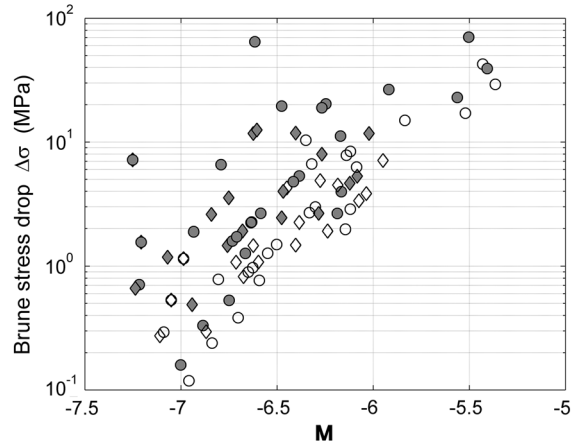


Figure 7

Estimates of moment magnitude M and Brune stress drop $\Delta\sigma$ derived from parameters t_0 and \dot{m}_{\max} obtained from waveform fitting for 48 LabEQs listed in Table 1 that are foreshocks (circles) or aftershocks (diamonds) of complete rupture events on a the 2 m-long simulated fault. Open symbols are original estimates and shaded symbols have been adjusted to account for attenuation and finite sensor aperture

amplitude of the LabEQs (\dot{m}_{\max}) rather than the frequency content (t_0). At a given corner frequency, M_0 varies by more than an order of magnitude.

Many of the estimated corner frequencies are close to or above the upper bound of the reliable frequency band of our recording system. At these

high frequencies, errors are introduced from the finite aperture of the sensor and attenuation in the granite, which would bias t_0 estimates to be somewhat larger than reality (a widening of farfield displacement pulses). We empirically tested the combined effects of sensor aperture and attenuation by comparing pulse widths estimated from ball drop calibration experiments to those expected from theory. A 1.00 mm glass ball dropped 1 m (Fig. 2) should theoretically have a pulse width of 2.9 μs , but the observed P and S wave farfield pulses were fit by a 4.5 μs pulse model. Similarly, a 1.58 mm steel ball should have 6.4 μs wide pulse width, but recorded signals were fit by a 7 μs pulse. Based on these observations, we apply an approximate correction factor to our t_0 estimates, which decreases our calculated M_0 and increases $\Delta\sigma$. These adjusted estimates (shaded symbols) are shown alongside unadjusted estimates (open symbols) in Fig. 7. This exercise indicates that at least some of the apparent scaling of stress drop with M_0 is an artifact of attenuation and sensor aperture effects described above.

Previous earthquake studies showed a similar apparent scaling of stress drop, (or, more commonly, apparent stress) with M_0 (e.g. GIBOWICZ *et al.* 1991), and this effect has been attributed to either attenuation, band limits of the recording system, or data selection bias (IDE and BEROZA 2001; IDE *et al.* 2003). We believe that the apparent scaling of stress drop with M_0 seen in the current study is also an artifact caused by unmodeled sensor aperture and attenuation effects which attenuate events with short rise time (high corner frequencies), but have only a small effect on events with lower corner frequencies which are in our reliable frequency band. The persistent lack of events with low $\Delta\sigma$ and large M_0 may be the result of our catalogue selection criterion that throws out events without clearly identifiable pulse-shaped direct P and S wave arrivals.

Figure 8 shows how the seismic moments and corner frequencies of the current dataset compare to natural and mining-induced earthquakes from five other studies. Taking into account the uncertainty noted above, and considering only events with corner frequencies that lie within our reliable frequency

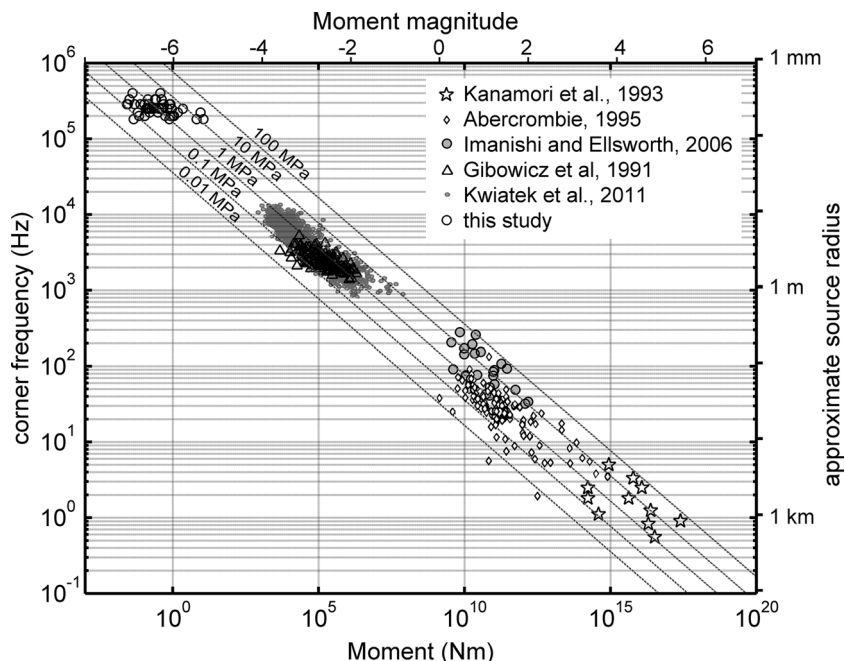


Figure 8

Corner frequencies and seismic moments of the LabEQS compared to events from five other studies of natural and mining-induced earthquakes. Approximate source radii and lines of constant stress drop (*dotted lines*) are based on the Brune model (see text) with $\beta = 3,300$ m/s. These parameters are model dependent and are only approximate, since β varies somewhat between the laboratory samples (2,700 m/s) and field estimates (3,300–3,700 m/s)

band, our estimates of Brune stress drop still lie in the 1–10 MPa range and show at least one order of magnitude spread in stress drops. As indicated by Fig. 8, even if a very modest scaling of stress drop with magnitude is fit to results from studies of larger earthquakes, when extrapolated down to the M -7 to M -5.5 events of the current experiments, such a scaling would predict stress drops that are many orders of magnitude higher or lower than the range estimated here. We, therefore, argue that the current data set is consistent with an earthquake model where stress drop does not vary systematically with seismic moment (AKI 1967; BRUNE 1970).

The stress drops estimated here are in some cases up to five times higher than the fault average normal stress. This observation coupled with the large spread in stress drops may indicate that considerable stress heterogeneity is present even on the relatively flat and smooth simulated fault.

6. Conclusions

The large scale laboratory apparatus employed in the current work provides observation conditions that are particularly conducive to the seismic analysis of tiny LabEQs radiated from the simulated fault. Utilizing high fidelity sensors and a rigorous treatment of wave propagation effects, we find that these events are well modeled by double couple focal mechanisms that are consistent with left lateral shear slip occurring on a mm-scale fault patch enclosed within the 2 m long simulated strike-slip fault cut through the granite sample.

Previous work on the same sample and apparatus indicated that these tiny LabEQs only occur when larger sections (>100 mm) of the fault undergo premonitory creep or afterslip at slip rates exceeding approximately 50 $\mu\text{m/s}$, and that high local stressing rates (~ 20 MPa/s) due to nearby aseismic slip were required for their existence (MCLASKEY and KILGORE 2013).

The current work is consistent with the above observations, but also shows that the seismic source characteristics of the M -7 to M -5.5 LabEQs are consistent with larger natural earthquakes, despite the unique circumstances for their existence. The short

(3–6 μs) rise times indicate corner frequencies in the hundreds of kHz range and source dimensions of a few mm. We find that the stress drops of these tiny LabEQs range from 1 to 10 MPa, which is entirely consistent with natural earthquakes of all sizes. Additionally, even on the relatively homogeneous laboratory fault, we observe more than an order of magnitude variability in LabEQ amplitude at a given corner frequency, which suggests more than an order of magnitude spread in stress drops at a given magnitude. The current experiments show that it is possible to create M -7 to M -5.5 seismic events in a laboratory that appear to be scaled versions of larger earthquakes. Careful study of such events could allow us to relate input parameters such as fault average stress state, loading conditions, and surface roughness to seismically observable source properties such as stress drop and radiated energy that are relevant to the physics of larger earthquakes.

Acknowledgments

This work benefitted from careful reviews by Art McGarr, Annemarie Baltay, and Grzegorz Kwiatek. The authors would also like to thank Brad Aagaard for assistance with the finite element modeling.

Appendix

Our estimates of seismic moment and stress drop are dependent on the absolute accuracy of the Green's functions, so we deemed it worthwhile to verify them by means of finite element modeling. We computed solutions to a 3D finite element model using the software PyLith (AAGAARD *et al.* 2013). Explicit dynamic finite element models useful for the computation of elastodynamic Green's functions become unstable when the number of elements per wavelength decreases to below about 10. The element size in our model is 3 mm, so the maximum frequency for S waves ($v_s = 2,700$ m/s) that our model can accommodate is about 90 kHz. Figure 9 shows synthetic seismograms obtained from the finite element model (thick grey lines) compared to synthetic seismograms obtained from the generalized ray

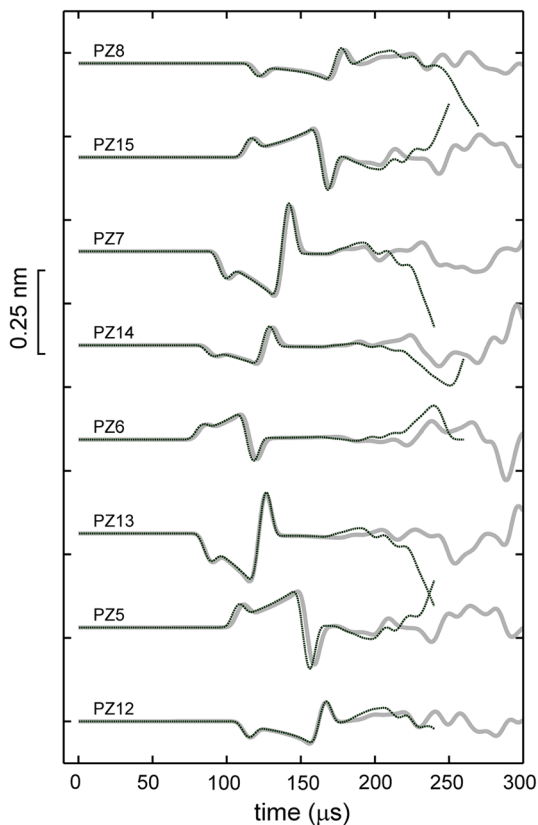


Figure 9

Comparison between synthetic seismograms obtained from our finite element model (*thick grey lines*) and synthetic seismograms obtained from the generalized ray theory code (*black dashed lines*), for the same source location as the LabEQ shown in Fig. 3 but different source duration. These synthetics include source and wave propagation components but do not include sensor distortions. The source term is a left-lateral strike-slip double couple focal mechanism with pulse-shaped moment rate function $\dot{m}(t)$ that is 15 μs wide and 85 kNm/s tall. Positive displacement is in the direction outward from the sample

theory code (black dashed lines) for the source and sensor geometries and orientations shown in Fig. 3. These synthetic seismograms are calculated exactly the same way as those shown in Fig. 3 except the instrument response function is not included and the width t_0 of a pulse-shaped moment rate function $\dot{m}(t)$ is set to 15 μs . This relatively wide pulse width (15 μs , corner frequency ~ 67 kHz) is required to keep the majority of the wave energy below our 90 kHz band limit, as set by the stability of the finite element model. The two solutions agree during the first part of the signals when only direct P and S waves and near field terms are present, and they

diverge at later times due to (1) errors associated with later arriving reflections in the generalized ray theory code, and (2) reflections off the sides of finite element model which are not accounted for in the infinite slab geometry of the generalized ray solution.

REFERENCES

- AAGAARD, B. T., KNEPLEY, M. G., and WILLIAMS, C., A. (2013) *A domain decomposition approach to implementing fault slip in finite-element models of quasi-static and dynamic crustal deformation*. *J. Geophys. Res.*, *118*, 3059–3079.
- ABERCROMBIE, R. E., (1995) *Earthquake source scaling relationships from -1 to 5 ML using seismograms recorded at 2.5-km depth*. *J. Geophys. Res.*, *100*, 24015–24036.
- AKI, K., (1967) *Scaling law of seismic spectrum*. *J. Geophys. Res.*, *72*, 1217–1231.
- BEELER, N. M., KILGORE, B., MCGARR, A., FLETCHER, J., EVANS, J., and BAKER, S. R. (2012) *Observed source parameters for dynamic rupture with non-uniform initial stress and relatively high fracture energy*. *J. Struct. Geol.*, *38*, 77–89.
- BOETTCHER, M. S., A. MCGARR, and M. JOHNSTON (2009), *Extension of Gutenberg-Richter distribution to M_w -1.3, no lower limit in sight*. *Geophys. Res. Lett.*, *36*, L10307, doi:10.1029/2009GL038080.
- BRACE, W. F. and J. D. BYERLEE (1966) *Stick slip as a mechanism for earthquakes*. *Science*, *153*, 990–992.
- BRUNE, J. N., (1970) *Tectonic stress and spectra of seismic shear waves from earthquakes*. *J. Geophys. Res.* *75*, 4997–5009.
- DIETERICH, J. H., (1981), *Potential for geophysical experiments in large scale tests*. *Geophys. Res. Lett.*, *8*, 653–656.
- DAHM, T. (1996) *Relative moment tensor inversion based on ray-theory: theory and synthetic tests*. *Geophys. J. Int.* *124*, 245–257.
- ELLSWORTH, W.L., HICKMAN, S.H., ZOBACK, M.D., IMANISHI, K., THURBER, C.H., ROECKER, S.W. (2007) *Micro- Nano- and Pico-earthquakes at SAFOD: Implications for Earthquake Rupture and Fault Mechanics*. *Eos (Transactions, American Geophysical Union)*, v. 88, no. 52, supplement, abstract S12B-05.
- GROSSE, C., REINHARDT, H, and DAHM, T. (1997) *Localization and classification of fracture types in concrete with quantitative acoustic emission measurement techniques*. *NDT & E International* *30*, 223–230.
- GROSSE, C., and OHTSU, M. *Acoustic Emission Testing* (Springer-Verlag: Berlin 2008).
- GIBOWICZ, S. J., YOUNG, R.P., TALEBI, S., and RAWLENCE, D. J. (1991) *Source parameters of seismic events at the Underground Research Laboratory in Manitoba, Canada: Scaling relations for events with moment magnitude smaller than -2* . *Bull. Seismol. Soc. Am.*, *81*, 1157–1182.
- GOEBEL, T., BECKER, T., SCHORLEMMER, D., STANCHITS, S., SAMMIS, C. RYBACKI, E., and DRESEN, G. (2012) *Identifying fault heterogeneity through mapping spatial anomalies in acoustic emission statistics*. *J. Geophys. Res.*, *117*, B03310.
- HSU, N. (1985), *Dynamic Green's functions of an infinite plate—A computer program*. *Tech. Rep. NBSIR 85-3234*, Cent. for Manuf. Eng., Natl. Bur. of Stand., Gaithersburg, Md.

- IMANISHI, K., and W. L. ELLSWORTH (2006), Source scaling relationships of microearthquakes at Parkfield, CA, determined using the SAFOD Pilot Hole Seismic Array, in *Earthquakes: Radiated Energy and the Physics of Earthquake Faulting*, Geophys. Monogr. Ser., vol. 170, (ed Abercrombie, R. et al.), pp. 81–90, AGU, Washington, D. C.
- IDE, S. and BEROZA, G. (2001) *Does apparent stress vary with earthquake size?* Geophys. Res. Lett. 28, 3349–3352.
- IDE, S., BEROZA, G., PREJEAN, S., ELLSWORTH, W. (2003) *Apparent break in earthquake scaling due to path and site effects on deep borehole recordings*, J. Geophys. Res. 108, B5, 2271.
- JOST, M. L., BÜBELBERG, T., JOST, Ö., and HARJES, H.-P. (1998) *Source parameters of injection-induced microearthquakes at 9 km depth at the KTB deep drilling site, Germany*, Bull. Seismol. Soc. Am., 88, 815–832.
- KWIATEK, G., PLENKERS, K., NAKATANI, M., YABE, Y., DRESEN, G., and JAGUARS-Group (2010) *Frequency-magnitude characteristics down to magnitude -4.4 for induced seismicity recorded at Mponeng gold mine, South Africa*, Bull. Seismol. Soc. Am. 100, 1165–1173.
- KWIATEK, G., PLENKERS, K., DRESEN, G. and JAGUARS Research Group (2011) *Source parameters of picoseismicity recorded at Mponeng deep gold mine, South Africa: implications for scaling relations*, Bull. Seismol. Soc. Am. 101, 2592–2608.
- LINZER, L. (2005) *A relative moment tensor inversion technique applied to seismicity induced by mining*, Rock Mech. Rock Engng. 38 (2), 81–104.
- LOCKNER, D. A., P. G. OKUBO, and J. H. DIETERICH (1982) *Containment of stick slip failures on a simulated fault by pore fluid injection*, Geophys. Res. Lett., 9, 801–804.
- LOCKNER, D. A., (1993) *Role of acoustic emission in the study of rock fracture*, Int. J. Rock Mech. Min. Soc. Geomech. Abstr., 30, 884–899.
- MANTHEI, G. (2005). *Characterization of acoustic emission sources in a rock salt specimen under triaxial compression*, Bull. Seismol. Soc. Am. 95, 1674–1700.
- MAXWELL, S. C., J. T. RUTLEDGE, R. JONES, and M. FEHLER (2010) *Petroleum reservoir characterization using downhole micro-seismic monitoring*, Geophysics, 75, 75A129–75A137.
- MCGARR, A. (1984). *Scaling of ground motion parameters, state of stress, and focal depth*, J. Geophys. Res. 89, 6969–6979.
- MCGARR, A. (1994). *Some comparisons between mining-induced and laboratory earthquakes*, Pure Appl. Geophys. 142, 467–489.
- MCGARR, A., (1999) *On relating apparent stress to the stress causing earthquake fault slip*, J. Geophys. Res., 104, 3003–3011, 1999.
- MCGARR, A., (2012) *Relating stick-slip friction experiments to earthquake source parameters*, Geophys. Res. Lett., 39, L05303.
- MCGARR, A., and FLETCHER, J. B. (2003) *Maximum Slip in Earthquake Fault Zones, Apparent Stress, and Stick-Slip Friction*. Bull. Seismol. Soc. Am. 93, 2355–2362.
- MCLASKEY, G., and GLASER, S. (2010) *Hertzian impact: experimental study of the force pulse and resulting stress waves*. J. Acoust. Soc. Am. 128, 1087–1096.
- MCLASKEY, G., and GLASER, S. (2011) *Micromechanics of asperity rupture during laboratory stick slip experiments* Geophys. Res. Lett., 38, L12302.
- MCLASKEY, G. and GLASER, S. (2012) *Acoustic Emission Sensor Calibration for Absolute Source Measurements*, J. Nondest. Eval. 31, 157–168.
- MCLASKEY, G. and KILGORE, B. (2013) *Foreshocks during the nucleation of stick-slip instability*, J. Geophys. Res. vol 118, 1–16.
- OHTSU, M. (1991), *Simplified moment tensor analysis and unified decomposition of acoustic emission: application to hydrofracturing test*, J. Geophys. Res. 96, 6211–6221.
- OKUBO, P., and DIETERICH, J. (1984), *Effects of physical fault properties on frictional instabilities produced on simulated faults*, J. Geophys. Res., 89, 5817–5827.
- PLENKERS, K., G. KWIATEK., and F. KRÜGER (2013) “Monitoring induced seismicity with AE sensors : the influence of unknown calibration functions,” in EGU General Assembly 7–12 April, 2013, Vienna, Austria. Abstract Number EGU2013-3849.
- PREJEAN, S. G. and ELLSWORTH, W. L. (2001) *Observations of earthquake source parameters and attenuation at 2 km depth in the Long Valley Caldera, Eastern California*, Bull. Seismol. Soc. Am., 91, 165–177.
- SELLERS, E. J., KATAKA, M. O. and LINZER L. M. (2003). *Source parameters of acoustic emission events and scaling with mining-induced seismicity*, J. Geophys. Res. 108, B9 2418.
- SHAH, K., and LABUZ, J. (1995) *Damage mechanisms in stressed rock from acoustic emission*. J. Geophys. Res., 100, 15,527–15,539.
- SPOTTISWOODE, S. M. and MCGARR, A. (1975) *Source parameters of tremors in a deep-level gold mine*, Bull. Seismol. Soc. Am. 65, 93–112.
- STANCHITS, S., VINCIGUERRA, S., and DRESEN, G. (2006) *Ultrasonic velocities, acoustic emission characteristics, and crack damage of basalt and granite*, Pure Appl. Geophys. 163, 974–993.
- THOMPSON, B. D., YOUNG, R. P. and LOCKNER, D. A. (2009), *Pre-monitory acoustic emissions and stick-slip in natural and smooth-faulted Westerly granite*, J. Geophys. Res., 114, B02205.
- ULRICH, T. J., MCCALL, K. R., and GUYER, R. A., (2002) *Determination of elastic moduli of rock samples using resonant ultrasound spectroscopy*, J. Acoust. Soc. Am. 111, 1667–1674.
- URBANCIC, T. Y., and TRIFU, C. (2000) *Recent advances in seismic monitoring technology at Canadian mines*, J. Appl. Geophys. 45, 225–237.
- WALTER, B. R., MAYEDA, K., and GOK, R. (2006) in *Earthquakes: Radiated Energy and the Physics of Earthquake Faulting*, Geophys. Monogr. Ser., vol. 170, (ed Abercrombie, R. et al.), pp. 25–41, AGU, Washington, D. C.
- ZANG, A., WAGNER, C., STANCHITS, S., DRESEN, G., ANDRESEN, R., and HAIDEKKER, M. (1998) *Source analysis of acoustic emissions in Aue granite cores under symmetric and asymmetric compressive loads*. Geophys. J. Int. 135, 1113–1130.